

**Spatial and Temporal Scales of Precipitating Tropical Cloud Systems in
Satellite Imagery and the NCAR CCM3**

Eric M. Wilcox

Center for Atmospheric Sciences, Scripps Institution of Oceanography,
University of California, San Diego, La Jolla, California

Submitted to *J. Climate*

April 30, 2002

Revised

November 27, 2002

Further revised

April 14, 2003

Corresponding author address: Eric Wilcox, Scripps Institution of Oceanography, University of California, San Diego, 9500 Gilman Dr., La Jolla, CA 92093-0221. (858) 534-1119, fax: (858) 534-7452. email: ewilcox@ucsd.edu.

ABSTRACT

Testing general circulation model parameterizations against observations is traditionally done by comparing simulated and observed, time-averaged quantities, such as monthly mean cloud cover, evaluated on a stationary grid. This approach ignores the dynamical aspects of clouds, such as their lifecycle characteristics, spatial coverage, temporal duration, and internal variability. In this study, a complementary Lagrangian approach to the validation of modeled tropical cloudiness is explored. An automated cloud detection and tracking algorithm is used to observe and track overcast decks of cloud in a consecutive set of hourly METEOSAT-5 images and the National Center for Atmospheric Research Community Climate Model version 3 (NCAR CCM3). The algorithm is applied to the deep convective cloud systems of the tropical Indian Ocean region during a 49 day period of the 1999 winter monsoon season. Observations of precipitation are taken from the Tropical Rainfall Measuring Mission (TRMM) satellite in addition to a METEOSAT-5 infrared rainfall technique that is calibrated using the TRMM data.

Clouds, defined as overcast decks, are observed spanning spatial scales from 25 km^2 to greater than 10^7 km^2 , as well as temporal scales from 1 hour to greater than 100 hours. Semi-permanent decks of anvil and cirrus cloud, with numerous regions of deep convection embedded within, dominate total cloud cover. Bridging between convective centers within the deck by cirrus cloud, particularly during the suppressed portion of the diurnal cycle of convection may help to maintain the integrity of semi-permanent overcast decks over long time scales. At scales greater than 10^6 km^2 the size distribution of simulated clouds is biased such that the dominant scale of clouds is several million square-kilometers larger than the dominant scale of observed clouds. Virtually all of the simulated precipitation occurs at rain rates lower than 2 mm hr^{-1} , while as much as 25% of observed precipitation occurs at rain rates higher than 2 mm hr^{-1} . Precipitation associated with deep convection in observed semi-permanent cloud systems is organized into more localized

mesoscale structures of adjacent convective cells attached to stratiform precipitation regions. A separate analysis of TRMM data (Wilcox and Ramanathan 2001) determined that such structures can exceed the size of grid cells in coarse-grid global models and have area-averaged rain rates up to and exceeding 2 mm hr^{-1} . These mesoscale convective systems are responsible for the extreme, episodic precipitation events that are not parameterized in the model. The simulated cloud systems gently precipitate throughout their duration and everywhere within their boundaries. The model lacks a process that acts to organize the convective cells within fewer grid cells, in addition to a representation of the observed stratiform precipitation structures. A modification to CCM3 is tested that is intended to account for the evaporation of upper-level precipitation in mid-level mesoscale downdrafts. The modification results in only a slight change in domain-averaged precipitation. However, it causes a significant shift in the distribution of precipitation toward higher rain rates that is more consistent with the distribution of TRMM observed rain rates. The modification demonstrates the sensitivity of the model to one important component of mesoscale organized convection.

1. Introduction

Condensed moisture, in the form of clouds and precipitation, is a key component of the climate system and continues to be a challenge for global models of the atmospheric general circulation. Latent heating from the condensation of precipitation is the largest source of heat driving atmospheric circulations. Variability of precipitation in time and space has important impacts on ecosystems and societies. Uncertainties in feedbacks associated with cloud cover and radiative forcing remain a leading source of uncertainty in greenhouse warming predictions (Houghton et al. 2001). Accurate, quantitative predictions of condensed moisture remain a challenge for global models because of their dependence upon processes, such as cumulus convection and thermodynamic phase changes, that often occur on time and space scales that are small relative to the time steps and grid cells of such models. Progress in this matter is further hindered by a lack of available observations across the necessary scales to constrain the problem.

Validation of the representation of moist processes in models is typically approached by means of Eulerian analysis schemes whereby time and space averages of simulated and observed quantities, such as surface rain rate or fractional cloud cover, are evaluated over stationary grids. Presented in this study is a Lagrangian analysis scheme, similar to the scheme developed by Boer and Ramanathan (1997), whereby the boundaries of clouds are identified and tracked in order to reveal the spatial and temporal scales of clouds and precipitation. This scheme was further refined to distinguish between precipitating and non-precipitating cloud systems by Wilcox and Ramanathan (2001). The analysis scheme is intended as a complement to the traditional Eulerian approach by identifying cases where the physical properties of cloud systems may be improperly simulated even when time- and space-averaged quantities agree with observations. Statistics are compiled and compared based on large ensembles of both observed clouds and modeled clouds whose properties,

such as spatial coverage, temporal duration and cloud-averaged precipitation rate, have been observed throughout the lifecycle of each cloud.

This study focuses specifically on clouds associated with the deep convective regime located over the tropical Indian Ocean during the winter monsoon season. Cloud observations are made using the METEOSAT-5 geosynchronous satellite. Rain rate estimates are also made using the infrared channel of METEOSAT-5 by means of a cloud-top temperature proxy that is tuned using simultaneous measurements from the TRMM satellite. Further comparisons of simulated and observed rain rate distributions are made using only TRMM data. The METEOSAT-5 imagery provide the ability to observe cloud systems spanning spatial scales from 25 km^2 to greater than 10^7 km^2 , and temporal scales as small as 0.5 hours. The observed cloud systems will be compared with simulated cloud systems from the NCAR CCM3 global atmospheric model.

As climate models evolve toward parameterization schemes that are more physically based, it should be expected that elements, such as clouds, which result from a combination of several independently parameterized processes, should accurately represent the behavior of complex, natural cloud systems. In regions of tropical deep convection, clouds arise primarily through the process of moist convection. The organization of convection into adjacent convective cells and mesoscale circulations (Houze and Betts 1981) results in precipitation structures that can exceed 10^6 km^2 (Wilcox and Ramanathan 2001). Convective updrafts transport condensate to the middle and upper troposphere where detrained condensate either precipitates, or remains suspended as large and persistent decks of cirrus cloud. Precipitating drops result from diffusion and coalescence within convective cells and the settling and melting of hail and graupel in mesoscale anvil circulations. Each of these processes is parameterized separately in GCMs, and the links between them are often absent. In this study the boundaries of clouds are chosen such that entire overcast cloud systems, including deep convection imbedded within extended cirrus decks, are grouped

together. Thus the analysis provides a test of how well simplified numerical representations replicate complete natural cloud decks that result from the linked processes listed above.

Increasingly, global GCMs are being coupled to chemical and aerosol transport models for the study and prediction of aerosol/climate interactions. For soluble species, the residence time in the atmosphere can be as short as 5-15 days because of the efficient removal by precipitation (Balkanski et al. 1993; Rasch et al. 2001). In this case it is crucial to validate the spatial and temporal distribution of precipitation at the scales of individual cloud systems. The following analysis identifies biases in the distribution of precipitation that may have significant implications for the simulated transport of soluble constituents.

2. Data and Methodology

Images from the METEOSAT-5 geosynchronous satellite are used to identify clouds, measure their sizes, estimate their area-averaged rain rates and track them in time. METEOSAT-5 provides half-hourly images from two channels in the infrared region of the spectrum and one in the visible. For this study, only brightness temperatures from the infrared window (IR) channel (10.5 - 12.5 μm) and the infrared water vapor band (WV) channel (5.7 - 7.1 μm) are used. The visible channel data is not used because clouds are tracked through the nighttime hours. The satellite was moved by the European Organization for the Exploration of Meteorological Satellites (EUMETSAT) to its present location above the equator at 63 degrees east longitude in support of the Indian Ocean Experiment (INDOEX). The raw data were gridded by EUMETSAT to a 5 km. \times 5 km. grid prior to being transferred to the INDOEX science team. The infrared window channel and water vapor channel images are distributed as digital counts which are converted to brightness temperatures (T_{IR} and T_{WV} respectively) using calibration coefficients provided by EUMETSAT. The coefficients are determined by comparing the counts to calculated radiances for

a subset of clear sky oceanic pixels where colocated reanalysis and radiosonde profiles are used as input to a radiative transfer model.

The bounds for this study are 40 to 120 degrees east longitude and -20 to 20 degrees latitude. METEOSAT-5 images from 1 Jan. through 18 Feb. 1999 are used. Calibration coefficients were not reported for six images during the period. For these cases, the coefficients from the previous image are used and visual inspection of the retrieved cloud maps indicated that the affected images fit smoothly into the context of the surrounding images. Following 18 Feb. 1999, contamination of the images by direct sunlight near local midnight resulted in gaps of several hours in the record, thus only the 49 day period between 1 Jan. and 18 Feb. is included in the study.

a. Pixel Classification and Cloud Detection

For the purposes of this study, a cloud is defined as a set of contiguous overcast pixels. In order to identify such regions in the METEOSAT-5 images, each pixel is placed in one of four classifications. Pixels with T_{IR} less than 240 K are labeled “deep convection/anvil”. Pixels with T_{IR} greater than 240 K and less than 280 K are labeled “shallow convection/thick cirrus”. Pixels with T_{IR} greater than 280 K and T_{WV} less than 245 K are labeled “thin cirrus”. All other pixels are assumed to be either clear sky or only partially covered by cloud and are disregarded in the following analysis. The classification scheme is summarized in Table 1.

Once the overcast pixels in an image have been identified and classified, a cloud clustering algorithm is applied whereby adjacent overcast pixels are grouped into a single cloud. Although a different algorithm is used here, the clustering scheme is identical to that described in Mapes and Houze (1993). Overcast pixels must share a side to be included in the same cloud.

Validation of the cloud detection algorithm has been performed using the NASA TRMM Visible Infrared Scanner (TRMM-VIRS) data (supplied using the CERES data products) for 10 days

of passes of the TRMM satellite that have been colocated with METEOSAT-5. The TRMM-VIRS data provide cloud cover fraction for 10 km (approximately) footprints derived from multi-spectral cloud imager data at 2 km resolution based on the techniques of Rossow and Garder (1993) and Stowe et al. (1991). The validation is performed from Jan. 21 – Jan. 31 (no data was available for Jan. 26) where only daytime TRMM passes are used in order to benefit from VIRS visible channel data. Colocation is performed by gridding the METEOSAT-5 and TRMM-VIRS data on the same 25 km grid. Over 75 000 colocated grid points are used in the comparison. Total cloud fraction for all colocated data points were in close agreement at 67% for the TRMM-VIRS data and 66% for the METEOSAT-5 cloud detection. All pixels identified as overcast by TRMM-VIRS were also identified as overcast by the METEOSAT-5. The largest errors in terms of discriminating partially filled grid cells from overcast grid cells occurred for cases where the TRMM-VIRS data indicated cloud cover greater than 80% and METEOSAT-5 misidentified them as overcast. This occurred in about 12% of cases, however results in small errors in terms of overall cloud cover, because TRMM-VIRS identified them as greater than 80% cloud cover. The largest errors in terms of identifying the boundaries and scales of clouds, as well as total cloud cover, probably occurs in grid cells with cloud fraction less than 10% that are misidentified as overcast by METEOSAT-5. This occurs in only about 4% of cases. Based on the close agreement in total cloud cover and the low incidence of mostly clear grid cells being misidentified as overcast, the METEOSAT-5 thresholds are reasonable for discriminating overcast decks of cloud. The separation of METEOSAT-5 pixels into the three classes indicated in Table 1 is intended to be mostly qualitative and is not compared with CCM3 output in this study. A separate validation of a cloud classification using similar IR and WV thresholds has been performed by Roca et al. (2002). They report that in addition to discriminating clear sky fraction to within 4% compared to a bispectral visible/IR scheme, the IR/WV thresholds determine thin cirrus coverage to within 1% compared to the visible/IR scheme.

b. Automated Cloud Tracking

Once cloud maps have been constructed for a series of consecutive images, an automated cloud tracking algorithm is applied to them based upon overlapping pixels in consecutive images. If a cloud overlaps at least one pixel from a cloud in the subsequent image, the two clouds are assumed to be related. Often, because of splitting, a cloud will overlap several clouds in the subsequent image. Likewise, a cloud often overlaps several clouds from the previous image because of merging. To determine which two clouds are the same cloud from a group of clouds related by overlap in two consecutive images, an “overlap parameter” is calculated for each pair of related clouds which is the product of the fractional area of each cloud that is overlapped. The pair of overlapping clouds with the largest overlap parameter is assumed to be the same cloud. This approach is chosen because it has the effects of identifying the pair of clouds with the maximum area of overlap, as well as the pair with the minimum change in area from one image to the next. Previous studies have tested several different decision algorithms designed to solve this problem and the results were found to be robust regardless of which decision algorithm is applied (Machado et al. 1998; Gambheer 2001). The overlap requirement means that fast moving, small-scale features may avoid tracking. For a single 5 km pixel feature, the required speed to avoid tracking would be only 5 km hr⁻¹. For larger features, however, the speed required to avoid tracking is much higher. Tracking schemes requiring an overlap constraint have been used successfully to track convective clusters that are likely to have maximum propagation speeds faster than the overcast decks tracked in this study (*e.g.*, Williams and Houze 1987).

Fig. 1a shows an example of a METEOSAT-5 IR-channel brightness temperature image. The same image, following the pixel classification stage is shown in Fig. 1b. The classification scheme is intended to be descriptive only and indicates the rough location of deep convection/anvil cloud, shallow convection/thick cirrus cloud, and thin cirrus. Fig. 1c shows the same image

following the cloud detection stage. The colors in Fig. 1c are chosen randomly and each color indicates a different cloud. The scene depicted in Fig. 1 is not uncommon during the winter monsoon season and shows a giant deck of overcast cloudiness oriented along the inter-tropical convergence zone with a number of smaller clouds at the periphery of the convergence zone. According to the analysis scheme employed in this study, the giant overcast deck is a single cloud and imbedded within this cloud are numerous regions of deep convection. Throughout this paper, the terms “cloud” and “overcast deck” will be used interchangeably to refer to the overcast features illustrated by the different colored features in Fig. 1c which are detected and tracked in the satellite imagery. The details of the cloud detection scheme were chosen to fulfill two goals: 1) to provide an objective means of identifying cloud boundaries that encompasses deep convective elements and their attached cirrus decks; and 2) to identify cloud elements in the satellite imagery that are comparable to cloud elements that may be identified in output from a global GCM. The definition of a cloud used here, and the cloud objects that result, is not intended to identify individual dynamical elements. Clearly the overcast deck indicated in blue in Fig. 1c includes several regions of convection that may be dynamically uncoupled. Furthermore, these convective regions are likely embedded in a cirrus deck that includes condensate that has detrained from the convective cores as well as cirrus associated with large-scale upper-tropospheric uplift that is not directly coupled to the convection. While a complete understanding of the dynamics giving rise to such cloud decks might warrant a more detailed separation of the overcast decks into smaller components, distinctions between these components cannot be made in the output of CCM3, as discussed further in section 2d. Clouds are therefore defined as overcast decks in order to distinguish individual objects in both the satellite imagery and the CCM3 output that are directly comparable. The resulting statistical description of overcast decks provides a test of the CCM3 cloud parameterization scheme that is appropriate for the level of complexity exhibited in the simulated cloud decks of the model.

c. IR Rain Rate Estimation

Surface rain rate estimates, averaged over the area of each cloud, are made using a variation of the GOES precipitation index (GPI) technique of Arkin and Meisner (1987). Rain rate (R_s , with units mm/hr) is related to f_{240} , the fraction of the area of each cloud with $T_{IR} < 240K$ according to the following expression:

$$R_s = Gf_{240}$$

where the coefficient, G , is calibrated by passive microwave rain rate measurements from colocated passes of the Tropical Rainfall Measuring Mission (TRMM) satellite (Kummerow et al. 1998). TRMM Microwave Imager (TMI) brightness temperatures are inverted to surface rain rates by means of the Goddard Profiling Algorithm (Kummerow et al. 2001). METEOSAT-5 and TRMM images are colocated in time and space by matching the METEOSAT-5 image nearest in time to the equator crossing time of each TRMM pass within the region, and both images are averaged over the same $0.25^\circ \times 0.25^\circ$ grid. Because of the high temporal sampling of METEOSAT-5, the colocated images differ in time by no more than about 15 minutes. The cloud classification and detection algorithm is applied to the METEOSAT-5 image and the fraction of each clouds' area that lies within the 760 km TRMM swath is noted. Only clouds with at least 20% of their area within the TRMM swath are used for calibrating the IR rain estimate. Furthermore, the area of the cloud captured by the TRMM swath must be at least $5 \times 10^4 \text{ km}^2$. The fraction of each clouds' area that is colder than 240K (f_{240}) and the TRMM rain rate are averaged over the area of the cloud contained within the swath. Nearly 350 clouds fit the above criteria. The relationship between area averaged rain rate and f_{240} for these clouds is shown in Fig. 2. The correlation coefficient between R_s and f_{240} is 0.7. G is determined by a least squares regression where the contribution of each point in Fig. 2 to the regression is weighted by the size of the cloud. G has the value 1.86 mm hr^{-1} according to the regression. Weighting the data by cloud size ensures that the domain-averaged value of R_s estimated

by METEOSAT-5 will agree reasonably well with that estimated by TRMM since the largest clouds contribute the most to the rainfall in the region. The domain-averaged rain rates (which are discussed in section 3) appear in Table 2. They are 3.31 mm day^{-1} for TRMM and 3.25 mm day^{-1} for METEOSAT-5. The METEOSAT-5 rain estimates are biased slightly low relative to TRMM because there is a small amount of precipitation observed from clouds that contain no cloud area colder than 240K. However, only about 2% of total precipitation observed by TRMM occurs in METEOSAT-5 identified clouds with $f_{240} = 0$. To the extent that TRMM may underestimate warm rain production (Kummerow et al. 2001), the 2% figure is a lower bound on the amount of rain occurring in clouds assumed not to be precipitating. Otherwise, the close agreement between the TRMM and METEOSAT-5 estimates reflects the tuning of G by the TRMM data.

Relationships between cold cloud fraction and precipitation, when averaged over sufficient temporal and/or spatial scales tend to be robust in spite of a poor correlation between rain rate and cloud-top temperature at the scale of satellite pixels. A discussion of techniques such as the one described above can be found in Atlas et al. (1990). In general, a greater amount of cold cloud-top coverage corresponds to a higher rain rate. However, a young growing convective cell can have a relatively warm cloud top, but a high rain rate. Alternatively, a decaying anvil cloud can have a cold cloud-top but a low rain rate. The IR rain estimate requires averaging over a sufficiently large area to capture an ensemble of cloud elements at various stages of the convective cloud lifecycle. Alternatively, small regions can be averaged over a sufficient period of time to capture the necessary variability. In this study, the emphasis will be on relatively large cloud systems; systems at least as large as a grid cell in a coarse global model. For these reasons, only clouds larger than $5 \times 10^4 \text{ km}^2$ are used in the calibration of the IR rain rate estimate. Averaging over an area of at least $5 \times 10^4 \text{ km}^2$ captures a sufficient ensemble of cloud elements to establish a reasonable correlation with

independent rain rate measurements, and further averaging tends not to improve the correlation (Richards and Arkin 1981).

Note that satellite estimates of surface rain rate are uncertain; in part because of a lack of an unambiguous ground truth. A complete analysis of the TRMM rain estimates appears in Kummerow, et al. (2001). They note that one comparison between instantaneous rain rates measured by TRMM and the radar located at the tropical station on Kwajalein suggests the TRMM measurements are biased low by 32%. An independent analysis, however, suggests a positive bias of 17%. Additional random error is introduced into the IR estimate due to the scatter in the relationship between R_s and G apparent in Fig. 2.

In addition to calibrating the IR rain rate estimate, TRMM measurements will be compared with the frequency distribution and domain average of simulated rain rates.

d. NCAR CCM3 simulation

The analysis of satellite imagery described above results in an ensemble of more than one million clouds spanning several orders of magnitude in spatial coverage and temporal duration. A companion ensemble of simulated clouds is generated for comparison using the National Center for Atmospheric Research Community Climate Model (NCAR CCM version 3.6.6; Kiehl et al. 1996 and 1998) run at T42 resolution (approx. $2.5^\circ \times 2.5^\circ$). The model is initialized with observations from 1 Sept. 1998 and run through 18 Feb. 1999. The period from 1 Sept. through 31 Dec. is included only to spin-up the model and is not used in the analysis. Observed monthly mean sea surface temperatures are applied. For comparison with the satellite imagery, only the Indian Ocean region (40-110 lon.; 20-20 lat.) is investigated. Overcast decks of cloud are identified in the model output by applying a threshold to the vertically integrated cloud fraction field (assuming random overlap) of 0.99. Clear-sky and partially filled grid cells are not used in the detection and tracking of simulated

clouds. The temporal and spatial scales of simulated clouds are relatively insensitive to the choice of cloud fraction threshold. Values between 80% and 99% were tested with little difference in the resulting statistics. Simulated cloud cover associated with the inter-tropical convergence zone during the winter monsoon is characterized by a strong gradient between grid cells with very high cloud fraction and adjacent grid cells of low cloud fraction.

In CCM3, the processes leading to the formation of cloud and precipitation arise from separate parameterizations. Layer clouds are formed using relationships based on relative humidity that are similar to those developed by Slingo (1987). Convective cloud cover is computed using a relationship based primarily on convective mass flux. In the tropical Indian Ocean region, the layer cloud parameterization provides most of the cloud cover, while the convective cloud amounts to a steady contribution of 10% low-level coverage in nearly all grid cells. The poor physical connection between convection, convective cloud cover, and anvil/cirrus layer cloud in the model is discussed by Rasch and Kristjánsson (1998). The spatial and temporal scales of CCM3 simulated tropical cloudiness are thus determined primarily by the resolved-scale distribution and transport of water vapor.

Given the important role of convection in generating condensate for convectively coupled cloud decks, as well as providing moisture for extended thin cirrus decks, investigations of the spatial scales of the convective cloud clusters embedded within the overcast decks addressed in this study is essential. Observations of the spatial scales of winter monsoon convective cloud clusters are presented in Roca and Ramanathan (2000) using geosynchronous satellite imagery using an algorithm developed by Boer and Ramanathan (1997) that distinguishes individual convectively generated cloud systems from low clouds or thin cirrus that may be dynamically unrelated to the convective system. The Boer and Ramanathan (1997) approach is not used in this study because the individual convective clouds are not distinguishable in the model output and therefore cannot be

directly compared with the resulting observations. This is partly due to the fact that many monsoonal convective cloud systems are smaller than a grid cell, though the largest cloud systems should be identifiable in model output as model resolution improves (Roca and Ramanathan 2000). As discussed in section 4, however, convection in CCM3 tends to be smoothed out in time and space, making individual convective systems indistinguishable. Furthermore, the layer cloud parameterization does not distinguish between cirrus cloud generated directly by convection and cirrus cloud that may result from other processes, such as large-scale upper-tropospheric uplift. As a result, further improvement of convection parameterizations, as well as improved physical links between the convection parameterization and simulated cloud cover, are required before individual convective clouds may be identified in model output. Once this is possible, comparisons such as presented here should be extended to the scales of individual convective clouds using more sophisticated approaches, such as that of Boer and Ramanathan (1997), as a test of the improved parameterizations.

Simulated precipitation in the tropical Indian Ocean region depends entirely on physics assumed to be occurring at subgrid-scales. Virtually all of the precipitation produced by the model in this region is generated within the deep convection parameterization scheme. According to the scheme, mass fluxes of a subgrid-scale ensemble of convective updrafts and downdrafts is predicted based on the quantity of convective available potential energy determined from grid cell values of temperature and humidity. Precipitation is produced at a rate that is proportional to the mass flux of the updrafts and a fraction of that precipitation is evaporated in the downdrafts. Details of the scheme are described in Zhang and McFarlane (1995). In winter monsoon cloud systems, approximately 97% of total precipitation results from deep convection. Another 2% of total precipitation is generated by a separate parameterization of shallow convection (Hack 1994). The

remainder is contributed through the process of stable condensation, whereby an entire grid cell reaches super-saturation and the excess moisture is removed as precipitation.

3. Domain-averaged precipitation and cloud cover

A comparison of the precipitation amount and cloud cover averaged over the entire observation region and time period is presented in Table 2. The domain averaged rain rate as observed by TRMM during the period is 3.31 mm day^{-1} . Using the infrared cloud-top temperature proxy for rain (calibrated by TRMM) the average rain rate is 3.25 mm day^{-1} . The model simulated rain rate during the same period is 5.31 mm day^{-1} ; or about 60% greater than observed. The amount of precipitation that occurs in grid cells that are partially filled with cloud is about 19% of the total model simulated precipitation in the domain. By collocating the METEOSAT-5 cloud mask and TRMM surface rain rate observations and averaging over the CCM3 grid, it is determined that 32% of observed precipitation occurs in partially filled grid cells. When observed rain rates are averaged over cloud area and arranged by cloud size, however, it is revealed that only about 2% of total precipitation results from clouds that are smaller than a single T42 model grid cell (not shown). This result suggests that it is common for the boundaries of intermediate-scale clouds and giant semi-permanent clouds to fall in the middle of a grid cell, and for that portion of the cloud to contain some precipitation. This result implies there is a limitation in the application of the cloud detection scheme to coarse-grid model output since all partially cloud covered grid cells are assumed to be composed of isolated clouds that are smaller than a grid cell, when in fact they include cloud cover that is attached to multi-grid cell overcast decks. Hence the spatial scales reported for CCM3 clouds are probably somewhat underestimated.

Cloud cover is substantially larger in the model simulation than in the observations. Model simulated cloud fraction is 66%. 52% is attributable to the overcast cloud decks tracked in this study, while 14% is contributed from partially filled grid cells. Observed cloud fraction is 45%,

suggesting that model overestimates cloud cover by 20%. Resampling the METEOSAT-5 images at the resolution of the model grid, indicates that the cloud cover associated with partially filled grid cells is 18%, which is in relatively close agreement with the model simulation. This suggests that the largest problems in simulating spatial coverage of cloud are associated with the overcast decks.

4. Spatial and temporal properties of cloud cover

The satellite image analysis indicates that a few, very large, semi-permanent overcast decks dominate winter monsoon cloud coverage over the Tropical Indian Ocean. Fig. 3a (solid line) shows the number distribution of observed clouds as a function of cloud lifetime. While over one million individual clouds were detected and tracked, only five clouds were found to last for greater than 100 hours. They are, however, the five largest clouds observed; each exceeding one million square-km in mean area, as illustrated in Fig. 3b (solid line). Mean area is defined as the area of the cloud averaged over each of the time steps through which the cloud was tracked. The cumulative contribution to the total observed cloud cover is presented in Fig. 3c and demonstrates that over 80% of the cloud coverage is attributable to just these five long lived clouds. Note that the lifetime of clouds is a somewhat arbitrary quantity because the birth and death of clouds, even at moderate scales, is predominantly determined by the merging and splitting of existing clouds rather than the spontaneous generation and dissipation of independent clouds. Nevertheless, the relationship between size and lifetime (Fig. 3b) indicates that, on average, the longevity and spatial coverage of clouds are positively correlated. A similar feature was observed for the convective clouds over the Pacific Ocean (Boer and Ramanathan 1997). Overcast decks reaching scales of tens of millions of square kilometers exist because the spatial scales of extended cirrus decks is sufficient to bridge the gaps between regions of intense deep convection. Such decks of cloud are able to persist for periods of weeks in spite of the faster time-scale variability of deep convection.

The diurnal variability of convection and extended decks of anvil and cirrus cloud are indicated in time series of cloud area for specific clouds. An example of the evolution of cloud area for a single tracked cloud appears in Fig. 4a. Figure 4b shows the area of the cloud that is attributable to each classification (the sum of each of the three lines in Fig. 4b is the curve shown in Fig. 4a). Deep convection and anvil cloudiness within this cloud tend to peak in the afternoon as illustrated by the area colder than 240K (solid line). The area covered by thin cirrus (dash-dot line) peaks 12-15 hours later and the intermediate cloud class (dashed line) peaks in between. While convection varies strongly on a diurnal time scale, a time lag between the peak in convection and the peak in cirrus cloud cover may explain how giant overcast decks persist for days to weeks. Time lags between active convection and the spatial coverage of resulting cloud decks observed in geostationary satellite imagery are discussed by Churchill and Houze (1984) and subsequently by Sherwood and Wahrlich (1999). Both studies address the evolution of individual convective structures (or composites of them as in Sherwood and Wahrlich, 1999), whereas the overcast cloud deck shown in Fig. 4 could be described as a cluster of such structures embedded within a larger region of overcast cloud cover. As noted by Sherwood and Wahrlich (1999), the evolution of cloud types within convective structures depends upon the scale of the structure. Furthermore, natural variability in the timescales of the evolution is apparent within size classes. They report a 4 hour lag between the area within the 235 K brightness temperature contour and the area within the 267 K contour in the largest mesoscale convective systems observed in the Western Tropical Pacific. This is somewhat shorter than the 7 hour lag between the peak in the deep convection/anvil cloud class and the shallow convection/thick cirrus apparent in Fig. 4d, which may reflect the warmer temperature threshold (280 K) used to distinguish the shallow convection/thick cirrus cloud class, compared to the 267 K threshold used by Sherwood and Wahrlich (1999).

A comparison of the evolution of cloud types in CCM3 to the METEOSAT-5 observations is particularly challenging because of the low vertical and horizontal resolution of global models, as well as the dominance of the layer cloud parameterization. Care must be taken that the cloud classifications assigned to model output accurately correspond to cloud classifications assigned to satellite brightness temperatures, and this has not been attempted here. Nevertheless, the satellite-observed and model-simulated cloud evolution should be reconciled, particularly as cloud parameterizations become more physically linked to convection and prognostic cloud water schemes become more commonplace. One promising approach to facilitating a comparison between the evolution of clouds in geostationary satellite imagery and model output is to simulate satellite imager brightness temperatures using cloud properties predicted by the model as demonstrated by Morcrette (1991) and Roca (2000). In this fashion, cloud classifications based on brightness temperature can be consistently applied to both the satellite data and model output.

Although cloud cover associated with overcast decks is over-predicted in CCM3, the comparison of modeled and observed temporal cloud statistics shown in Fig. 3 indicates good agreement (all results for model simulated clouds are shown with dotted lines). Differences in the number distribution and mean area of clouds at time scales of 1 hour to 1 day result from the difference in resolution between the model grid and the satellite imagery. The horizontal dashed line in Fig. 3b indicates the approximate size of a single model grid cell. There cannot be any overcast decks in the model that are smaller than a grid cell. Because of the finer resolution of the satellite, there are overcast decks identified in the imagery that are smaller than the model grid cell. In fact, there are a large number of these observed subgrid-scale clouds, which tend to have lifetimes shorter than a day. These clouds, if present in the model, are excluded from the cloud detection and tracking analysis. Hence the appearance of a larger number of short-lived subgrid-scale clouds in the observations is an artifact of the analysis scheme. When the data are expressed as the cumulative

contribution to total cloud cover (Fig. 3c), the dominance of the giant, semi-permanent overcast decks is apparent in both the satellite imagery and the model simulation.

That the model is capable of reproducing the presence of the semi-permanent decks is noteworthy because the model does not impose any time scales on the cloud cover. In the standard configuration, the model completely erases and recalculates the cloud field once each model hour. Since relative humidity is the sole predictor of the upper-level clouds that make up the semi-permanent cloud decks, this result implies that the time scales associated with the large-scale distribution of humidity and the moisture transport are appropriate for maintaining the cloud decks.

As mentioned above, however, cloud fraction associated with the semi-permanent decks is too large, which is attributable to an improper representation of the spatial scales of these cloud systems. Fig. 5a shows the number distribution of clouds as a function of cloud size for observed and simulated clouds. The observations indicate that there are many orders of magnitude more clouds at the scale of a satellite pixel than there are at the scales of 10^6 to 10^7 km². The distribution of model simulated clouds indicates that there are too many clouds at the intermediate scales of one to a few grid cells, too few clouds between 10^6 and 10^7 km² and too many clouds at scales of the largest overcast decks.

In order to assess how the number distribution as a function of size may depend upon the criteria used to identify the boundaries of overcast decks, an inset is included in Fig. 5a comparing distributions resulting from clouds identified in the METEOSAT-5 imagery, 23 days of TRMM-VIRS multi-spectral data from Jan. 1999, and 38 days of TRMM-CERES broadband shortwave flux data from winter 1998 published previously (Wilcox and Ramanathan, 2001). Because the absolute number of clouds observed depends upon the total amount of area observed, which is different in each data set, the distributions are normalized by the number of clouds in the 5×10^4 km² size bin.

The inset shows that up to the 10^6 km^2 scale, two independent measures from the polar-orbiting TRMM data observe a size distribution of clouds comparable to that observed by the METEOSAT-5 geostationary data. However, the sizes of clouds larger than 10^6 km^2 cannot be properly measured with polar-orbiting data because they extend beyond the edges of the swath.

The consequence of the model bias in the size distribution of clouds is evident in Fig. 5b, which shows the cumulative contribution to total cloud cover as a function of cloud size. The dominant scale of clouds, those that contribute to most of the total cloud cover, is several million square-km larger in the model. This result implies that either the upper-tropospheric humidity is distributed too broadly over the region during too much of the period, or the diagnostic relationship between relative humidity and cloud fraction is biased toward too much cloud for winter monsoon anvil and cirrus cloud.

5. Observed and simulated precipitation properties

Across the observed scales of clouds, precipitation rate increases with cloud size. In contrast, simulated clouds exhibit a nearly binary behavior with respect to precipitation (Fig. 6a). Simulated clouds smaller than $2 \times 10^6 \text{ km}^2$ have cloud area-averaged rain rates of about 0.15 mm hr^{-1} , while clouds larger than $2 \times 10^6 \text{ km}^2$ have rain rates of about 0.35 mm hr^{-1} . Because of the large space and time scales of the largest clouds, they dominate the contribution to the domain-averaged precipitation. The over-prediction of rain rate within clouds at the largest scales, is responsible for the over-prediction of precipitation over the entire domain and time period.

Although the intermediate-scale clouds ($5 \times 10^4 \text{ km}^2$ to $5 \times 10^5 \text{ km}^2$) have average rain rates in better agreement with observed rain rates, the fraction of clouds at this scale that are precipitating is slightly overestimated, as indicated by Fig. 6b. Here the probability that a cloud contains a region of precipitation within its boundaries is presented as a function of cloud size. The

giant, semi-permanent cloud decks always contain active deep convection, and are therefore always precipitating. The smallest observed clouds (less than $1 \times 10^5 \text{ km}^2$) almost never precipitate. A fraction ranging between 0.4 and 1 of the intermediate-scale clouds are precipitating clouds. This includes a fraction of clouds that never precipitate as well as a fraction of clouds that precipitate for only a portion of their total lifetime.

While precipitation averaged over the horizontal scales of giant cloud decks is larger than observed, rain rates on the scale of individual grid cells is biased low relative to observations. This is confirmed by directly comparing the frequency distribution of simulated grid cell rain rates to measured rain rates averaged over the same CCM3 model grid. Because rain rates estimated by infrared brightness temperatures are less accurate than passive microwave measurements, only TRMM measurements are used here. All TRMM passes over the Indian Ocean region during the 49 day period are used and the pixel data are averaged over the CCM3 grid cells at T42 resolution. The result is shown in Fig. 7 (solid and dotted lines). Virtually all of the simulated precipitation occurs at instantaneous rain rates lower than 2 mm hr^{-1} , while as much as 25% of the observed precipitation occurs at rain rates higher than 2 mm hr^{-1} . Furthermore, greater than 99% of the simulated precipitation is diagnosed by the convective parameterization scheme and hence is assumed to result entirely from convective updrafts at scales much smaller than a single grid cell. This means that less than 1% of the precipitation occurs by the stable condensation process, whereby an entire grid cell reaches super-saturation and the excess moisture is removed as precipitation. However, application of the cloud clustering algorithm directly to the surface rain rate images from TRMM indicates that 60% of observed precipitation in the region occurs in contiguous regions of precipitation that are larger than a single T42 model grid cell (not shown). The horizontal scale of rain areas and the horizontal scale of a resolved dynamical feature necessary to produce a supersaturated grid cell are probably not comparable. Nevertheless, the observations reveal that a significant portion of

precipitation in the winter monsoon environment results from mesoscale organized convective structures spanning areas larger than a model grid cell. Such structures are not parameterized in the model, yet the model resolution is not sufficient for motions at these scales to emerge. These mesoscale convective systems are responsible for the extreme, episodic precipitation events at the tail of the TRMM rain distribution in Fig. 7. Such systems are typically embedded within larger cloud decks with as much as 75% of the cloud deck consisting of non-precipitating cloud (Wilcox and Ramanathan 2001). In contrast, the simulated clouds gently precipitate everywhere and all of the time.

The smoothing of precipitation in time and space in the model has obvious implications for the prediction of extreme precipitation events. The effects on simulations of the atmospheric circulation and hydrological cycle in regions of deep convection require further study. The poor representation of the time and space scales of precipitation may also have important implications for the evolution of soluble trace gas and aerosol constituents. The transports of such constituents are now commonly added to global general circulation models in order to assess their climate impacts. The distribution of such constituents is often quite heterogeneous. Subjecting them to a scavenging loss mechanism that is improperly represented in time and space could potentially lead to large errors in predictions of their concentrations.

6. Sensitivity of simulated rain rate distribution to moisture recycling

The broad distribution of gentle precipitation in CCM3 is a consequence of a tendency within the convective parameterization scheme to neutralize instability too frequently. Similarly, the complete dominance of convective precipitation over stable condensation results from the too frequent invocation of the convection scheme. A reformulation of the convective parameterization is beyond the scope of this paper. However, a simple modification to the parameterization of convective precipitation in the model is tested here that simulates the effect of the evaporation of

convectively generated precipitating condensate in mesoscale downdrafts. The modification has a significant impact on the frequency distribution of rain rate.

In the standard formulation of CCM3, convective precipitation is diagnosed from the magnitude of convective mass flux (Zhang and McFarlane 1995). Under the assumption that all of evaporation of precipitation occurs within narrow saturated downdrafts, a portion of the diagnosed precipitation is allowed to re-evaporate. In the case of tropical convection, however, as much as 16% of the total precipitation in a mesoscale cloud cluster may be evaporated in unsaturated mesoscale downdrafts (Gamache and Houze 1983). As mentioned previously, the physics of these mesoscale organized convective structures are absent from the present formulation of convection in CCM3. In this section, a simple modification is made to CCM3 that allows a fraction of the convective precipitation to re-evaporate within the environment surrounding the convective updrafts and downdrafts. This modification is not intended to be a complete parameterization of organized tropical convection, as it does not include many important features, such as the mass and momentum fluxes within mesoscale updrafts and downdrafts. The modification does, however, illustrate the potential importance of environmental moistening by such structures in modulating the spatial and temporal scales of precipitation. Note that evaporation scheme applied here is similar to a scheme that will be included in the next version of CCM3 and is present in other GCMs.

Parameterized mesoscale re-evaporation is limited only to precipitation generated through the parameterization of deep convection. Following the formulation of the re-evaporation of stable condensation, which is already present in the model, deep convective precipitation is made available for evaporation in each lower layer where relative humidity is less than 1. Unlike stable condensation, however, evaporation of deep convective precipitation is further constrained by the cloud field. In addition to being sub-saturated, grid cells must have a cloud fraction less than 0.5 for deep convective precipitation to evaporate. The cloud fraction constraint is chosen arbitrarily,

however is designed to be consistent with the observation that mesoscale evaporation occurs in clear areas beneath precipitating anvils. Like the evaporation of stable condensation, the rate of evaporation of deep convective precipitation is calculated using the relation proposed by Sundqvist (1988):

$$E = k_E (1 - RH) R^{1/2}.$$

E is the rate of the evaporation, RH is relative humidity and R is the rate of production of precipitation. E has the units of kg/kg s^{-1} and R has units of $\text{kg m}^{-2} \text{s}^{-1}$. The constant, k_E , has the value 10^{-5} . For grid columns in the Indian Ocean region with rain rates greater than 1 mm hr^{-1} this formulation results in a vertically integrated evaporation rate that is on average about 10% of the surface rain rate, which is in reasonable agreement with the observational study of Gamache and Houze (1983).

Domain-averaged rain rate remains nearly constant (5.39 mm day^{-1} compared to 5.31 mm day^{-1}) in spite of the increased evaporation, indicating that the overall quantity of moisture removed from the Indian Ocean monsoon trough is somewhat insensitive to the details of precipitation microphysics. The distribution of precipitation, however, changes significantly. The addition of parameterized mesoscale evaporation shifts the distribution of winter monsoon precipitation toward higher rain rates than in the standard CCM3 simulation (Fig. 7, dashed lines). While almost no simulated precipitation occurs at rates higher than 2 mm hr^{-1} in the standard model, nearly 20% of the total precipitation occurs in grid cells with rain rates greater than 2 mm hr^{-1} in the modified model. The addition of moisture recycling also results in a modest increase in the percentage of precipitation resulting from stable condensation; rising from 1% in the standard simulation to 3% in the modified simulation. As discussed previously, observations of the horizontal scales of surface rain rate features suggest that the stable condensation fraction should be higher than in the standard

model, however the proper value of this partitioning is not well constrained by observations. Better observations of the vertical profile of precipitating condensate would help in this regard.

Furthermore, the value of this partitioning should be closely tied to the convective parameterization, which in turn should be properly tuned to the resolution of the model, since the amount of stable condensation will reflect the amount of resolved-scale convection is assumed to be present.

The modification to the model tested here is intended to determine if a simple modification to the model could significantly change the distribution of precipitation. The increased frequency of extreme rain events occurs because of an increase in the lower tropospheric humidity, which is most prevalent in the regions where convection is already occurring, because that is where the evaporation is applied. This increases the convergence of moisture in grid columns already undergoing convection. Enhanced convergence of moisture at the scale of individual storm systems has been suggested as a mechanism for the increased frequency of extreme precipitation events that occurs in simulations of enhanced greenhouse forcing (Trenberth 1998). While successful in generating extreme precipitation rates more similar to the observations, the modification is not intended to account for the mass, momentum and energy fluxes associated with organized mesoscale convection. A discussion of the effects of a more complete parameterization of mesoscale dynamics on many aspects of a GCM integration can be found in Donner et al. (2001).

7. Summary

A Lagrangian analysis scheme is explored as a tool for testing the spatial, temporal and precipitation characteristics of winter monsoon clouds over the tropical Indian Ocean as simulated by the NCAR CCM3 global general circulation model. Overcast decks of cloud of the scale of a single model grid cell and larger are detected and tracked over a 49 day period during January and February, 1999 and compared with clouds observed by the METEOSAT-5 geosynchronous satellite. Statistics for simulated and observed clouds are arranged by size and lifetime in order to determine if

the frequency distribution of clouds as a function of size and lifetime are properly simulated. Furthermore, the dependence of rain rate and rain frequency upon cloud size is compared, where infrared rainfall estimates are supplemented with colocated observations from the TRMM satellite. Such Lagrangian statistics supplement more traditional Eulerian techniques of comparing time- and space-averaged, gridded fields of cloud cover and precipitation in determining where model parameterizations fall short of simulating complex deep convective cloud systems.

Note that the Jan. 1 – Feb. 18 1999 period spanned by this study coincides with one complete Madden-Julian Oscillation. Convective activity is building during the early part of January and peaks about January 23. Convective activity then decreases, and is suppressed during the first part of February, before building again following the Feb. 18 ending date of this study. The strength of this oscillation, in terms of intraseasonal variability of outgoing longwave radiation, is not particularly strong or weak relative to other years, although the timing of the Jan. 23 peak in the area influenced by convective activity is unusual (J.-P. Duvel, personal communication).

Clouds, defined as overcast decks, are observed spanning spatial scales from 25 km^2 to greater than 10^7 km^2 ; as well as temporal scales from 1 hour to greater than 100 hours. Semi-permanent decks of anvil and cirrus cloud, with numerous regions of deep convection embedded within, dominate total cloud cover. The peak in the spatial coverage of cirrus cloud lags the peak in coverage by deep convective cloudiness by 12-15 hours, acting to bridge the regions between convective centers. As a result, semi-permanent cloud decks can persist for time scales of days to weeks. It is potentially advantageous for global models with coarse grids that overcast decks as large or larger than several model grid cells dominate deep convective cloud cover. From a validation standpoint, this fact means there are identifiable cloud features (*i.e.*, resolved overcast decks) that can be directly compared to similar observable features. Semi-permanent decks are simulated in CCM3 in spite of the fact that the diagnostic scheme for predicting cloud cover makes no assumptions

about the time scales of cloud material. Nevertheless, several significant differences are apparent between the observed and simulated cloud systems.

At scales greater than 10^6 km² the size distribution of simulated clouds is biased such that the dominant scale of clouds is several million km-square larger than the dominant scale of observed clouds. Averaged over the entire domain, cloud cover attributable to the giant overcast decks is over-predicted by greater than 20%. In order to maintain cloud decks of this scale, precipitating deep convection is always occurring somewhere within the boundaries of the cloud. These cloud systems also contribute most of the precipitation in the region. Within the simulated semi-permanent decks, precipitation rates averaged over cloud area are substantially higher than observed. As a result, the domain-averaged precipitation rate is larger in the model simulation than is observed by the TRMM satellite. Although precipitation is over-predicted in the model, the frequency distribution of rain rates is biased low in the model relative to TRMM data averaged over the model grid. The semi-permanent cloud decks simulated in the model gently precipitate throughout their duration and everywhere within their boundaries. This contrasts with observed semi-permanent cloud systems, which precipitate throughout their duration, but do so in more localized regions of precipitation with non-precipitating regions of cloud between. Most of the observed precipitation occurs in mesoscale precipitation features with high precipitation rates that are absent from the model. All of the simulated precipitation occurs in convective updrafts assumed to be small relative to a model grid cell. What the model lacks is a process that acts to organize the convective cells within fewer grid cells, in addition to a representation of the observed stratiform precipitation structures. Furthermore, while most grid cells within the semi-permanent clouds are precipitating, very few reach grid cell supersaturation and precipitate by stable condensation. The scales of saturated regions cannot be observed, however the TRMM imagery indicates that as much as 60% of precipitation results from precipitation regions that are larger than a single grid cell. This implies

that a greater fraction of simulated precipitation should arise from stable condensation, although more detailed observations are required to properly constrain this parameter.

On average, intermediate-scale clouds (clouds of the size of one to a few grid cells) have precipitation rates that are similar to observed clouds of comparable scale. However, the probability that a cloud at this scale contains some precipitation is slightly overestimated in the model. Cloud cover associated with partially filled grid cells in the model agrees reasonably well with observed clouds averaged over the model grid. Evidence suggests that a significant portion of the partially filled grid cells are in fact attached to overcast decks that are larger than a grid cell. 19% of simulated precipitation and 32% of observed precipitation occurs in model grid cells that are only partially filled with cloud. Clouds that are physically smaller than a model grid cell are plentiful in the observations, however, they account for a small portion of the total cloud cover and only 2% of precipitation observed by TRMM.

As the application of general circulation models expands to the simulation and prediction of precipitation variability of societal importance, such as the frequency of extreme precipitation events, the biases in the distribution of rain rates documented here will become an increasingly serious issue. Even in cases where analyses of simulated monthly mean precipitation fields indicate quantitative and spatial agreement with observations, the intense precipitation events associated with organized mesoscale structures are missing. Likewise, the use of global GCMs to drive the advection and scavenging of aerosols will require that the spatial and temporal scales of precipitation be adequately represented. The application of the Lagrangian analysis scheme employed in this study to satellite imagery of clouds and precipitation can help constrain assumptions within aerosol scavenging parameterizations about the spatial scales of precipitation.

Convection parameterizations that include the organization of deep convection, and associated mesoscale circulations, may help generate the extreme precipitation events not presently found in CCM3. In this study, a modification to CCM3 is tested that is intended to account for the evaporation of upper-level precipitation in mid-level mesoscale downdrafts. The modification results in only a slight change in domain-averaged precipitation, indicating that the regional-scale hydrological balance is not sensitive to this aspect of convection. However, it causes a significant shift in the distribution of precipitation toward higher rain rates, as well as a modest increase in the fraction of precipitation resulting from stable condensation. The modification demonstrates the sensitivity of the model to one important component of mesoscale organized convection. Further testing with more complete parameterizations of mesoscale convection, including representations of additional processes such as mesoscale mass fluxes and anvil cloud microphysics, should be performed. Attention should be paid to how such processes impact quantities such as instantaneous rain rate and cloud scales, in addition to time- and space- averaged climate. For example, a more complete representation of phase changes associated with mesoscale circulations may impact the upper-tropospheric water budget and the spatial scales of simulated cloud decks.

The analysis presented here needs to be extended globally in order to completely document the extent of the model biases found here and the specific regions and meteorological regimes effected by them. Comparisons between simulated and observed cloud systems should include time- and space- averaged quantities, such as monthly mean cloud cover and precipitation, as well as instantaneous quantities, such as the spatial scales of cloud systems and instantaneous rain rates. For example, global climate models, such as CCM3 are used to investigate the response of the hydrological cycle to enhanced greenhouse forcing (*e.g.*, Roads et al. 1996). Increases in accumulated regional precipitation, in conjunction with an increase in the frequency of extreme instantaneous, storm-scale precipitation events, is a common response in GCMs to enhanced greenhouse forcing

(Trenberth 1998). In the simulated winter monsoon, however, accumulated regional precipitation is biased high while instantaneous, storm-scale rain rates are biased low. This result highlights the need to test models at multiple scales.

An advantage of the Lagrangian analysis scheme is that it evaluates clouds and precipitation in the context of integrated cloud systems. Convection, clouds and microphysics are parameterized separately in GCMs. In nature, however, close coupling between each of these processes gives rise to the cloud systems observed in satellite imagery. Not every applicable quantity is observable, however the Lagrangian scheme provides a means of evaluating how well the links between each of the parameterized processes result in cloud systems that mimic natural cloud systems. This study has explored some of the relationships between precipitation and cloud cover. The analysis demonstrates that there is a mismatch between the distribution of precipitation and the distribution of cloud cover: most seriously within the giant semi-permanent decks. In spite of the fact that convective-scale and mesoscale updrafts provide the condensate for both the precipitation and the extended decks of cloud, the relative humidity-based cloud cover parameterization is physically decoupled from convection in the model. The resulting cloud cover associated with the semi-permanent decks is higher than observed and precipitation is not properly distributed in time and space within the clouds.

Acknowledgments. METEOSAT-5 data were provided by EUMETSAT in support of the INDOEX field experiment. TRMM TMI data were provided by the NASA Goddard Space Flight Center Distributed Active Archive Center (DAAC). CERES data were provided by the NASA Langley Research Center DAAC. The author wishes to thank V. Ramanathan for discussions and useful suggestions throughout the course of this project, Guang Zhang and Phil Rasch for helpful discussions regarding CCM3 parameterizations, Chul Eddy Chung for assistance setting up the model, and Jean-Philippe Duvel and Rémy Roca for sharing the results of their multi-year analysis of

the intraseasonal oscillation of OLR. This research has been supported by NASA-CERES grant NAS5-NAS1-98141. This is Center for Clouds, Chemistry and Climate (C⁴) report #261.

REFERENCES

- Arkin, P. A. and B. N. Meisner, 1987: The relationship between large-scale convective rainfall and cold cloud over the western hemisphere during 1982-84. *Mon. Wea. Rev.*, **115**, 51-74.
- Atlas, D., D. Rosenfeld, and D. A. Short, 1990: The estimation of convective rainfall by area integrals 1. The theoretical and empirical basis. *J. Geophys. Res.*, **95**, 2153-2160.
- Balkanski, Y. J., D. J. Jacob, G. M. Gardner, W. C. Graustein, and K. K. Turekian, 1993: Transport and residence times of tropospheric aerosols inferred from global three-dimensional simulation of ^{210}Pb . *J. Geophys. Res.*, **98**, 20 573-20 586.
- Boer, E. R. and V. Ramanathan, 1997: Lagrangian approach for deriving cloud characteristics from satellite observations and its implications to cloud parameterization. *J. Geophys. Res.*, **102**, 21 383-21 399.
- Churchill, D. D. and R. A. Houze Jr., 1984: Development and Structure of Winter Monsoon Cloud Clusters on 10 December 1978. *Mon. Wea. Rev.*, **41**, 933-960.
- Donner, L. J., C. J. Seman, R. S. Hemler, and S. Fan, 2001: A cumulus parameterization including mass fluxes, convective vertical velocities, and mesoscale effects: thermodynamic and hydrological aspects in a general circulation model. *J. Climate*, **14**, 3444-3463.
- Gamache, J. F. and R. A. Houze Jr., 1983: Water budget of a mesoscale convective system in the tropics. *J. Atmos. Sci.*, **40**, 1835-1850.
- Gambheer, A. V. and G. S. Bhat, 2000: Life cycle characteristics of deep cloud systems over the Indian region using *INSAT-1B* pixel data. *Mon. Wea. Rev.*, **128**, 4071-4083.

- Hack, J. J., 1994: Parameterization of moist convection in the National Center for Atmospheric Research Community Climate Model (CCM2). *J. Geophys. Res.*, **99**, 5551-5568.
- Houghton, J. T., Y. Ding, D. J. Griggs, M. Noguer, P. J. van der Linden, and D. Xiaosu, Eds., 2001: *Climate Change 2001: The Scientific Basis: Contribution of Working Group 1 to the Third Assessment Report of the Intergovernmental Panel on Climate Change*. Cambridge University Press, 944 pp.
- Houze, R. A. and A. K. Betts, 1981: Convection in GATE. *Rev. Geophys. Space Phys.*, **19**, 541-576.
- Kiehl, J. T., J. J. Hack, G. B. Bonan, B. A. Boville, D. L. Williamson, and P. J. Rasch, 1998: The National Center for Atmospheric Research Community Climate Model: CCM3. *J. Climate*, **11**, 1131-1149.
- Kiehl, J. T., J. J. Hack, G. B. Bonan, B. A. Boville, B. P. Briegleb, D. L. Williamson, and P. J. Rasch, 1996: Description of the NCAR Community Climate Model (CCM3). NCAR Tech. Note, NCAR/TN-420+STR, 151 pp. [Available from National Center for Atmospheric Research, Boulder, CO 80307; <http://www.cgd.ucar.edu/cms/ccm3/TN-420/>].
- Kummerow, C., W. Barnes, T. Kozu, J. Shiue and J. Simpson, 1998: The Tropical Rainfall Measuring Mission (TRMM) sensor package. *J. Atmos. Ocean Technol.*, **15**, 809-817.
- Kummerow, C., Y. Hong, W. S. Olson, S. Yang, R. F. Adler, J. McCullum, R. Ferraro, G. Petty, D. - B. Shin and T. T. Wilheit, 2001: The evolution of the Goddard Profiling Algorithm (GPROF) for rainfall estimation from passive microwave sensors. *J. Appl. Meteor.*, **40**, 1801-1820.
- Machado, L. A. T., W. B. Rossow, R. L. Guedes, and A. W. Walker, 1998: Life cycle variations of mesoscale convective systems over the Americas. *Mon. Wea. Rev.*, **126**, 1630-1654.

- Mapes, B. E. and R. A. Houze, 1993: Cloud clusters and superclusters over the oceanic warm pool. *Mon. Wea. Rev.*, **121**, 1398-1415.
- Morcrette, J. J., 1991: Evaluation of Model-generated Cloudiness: Satellite-observed and Model-generated Diurnal Variability of Brightness Temperature. *Mon. Wea. Rev.*, **119**, 1205-1224.
- Rasch, P. J. and J. E. Kristjánsson, 1998: A comparison of the CCM3 model climate using diagnosed and predicted condensate parameterizations. *J. Climate*, **11**, 1587-1614.
- Rasch, P. J., W. D. Collins, and B. E. Eaton, 2001: Understanding the Indian Ocean Experiment (INDOEX) aerosol distributions with an aerosol assimilation. *J. Geophys. Res.*, **106**, 7337-7355.
- Richards, F. and P. Arkin, 1981: On the relationship between satellite-observed cloud cover and precipitation. *Mon. Wea. Rev.*, **109**, 1081-1093.
- Roads, J. O., S. Marshall, R. Oglesby, and S.-C. Chen, 1996: Sensitivity of the CCM1 hydrologic cycle to CO₂. *J. Geophys. Res.*, **101**, 7321-7339.
- Roca, R. and V. Ramanathan, 2000: Scale Dependence of Monsoonal Convective Systems over the Indian Ocean. *J. Climate*, **13**, 1286-1289.
- Roca, R., 2000: Validation of Cloudiness in GCMs Using METEOSAT Observations. *Proc. Of the ECMWF/Euro TRMM Workshop on the Assimilation of Clouds and Precipitation*, Reading, United Kingdom, ECMWF.
- Roca, R., M. Viollier, L. Picon, and M. Desbois, 2002: A multi-satellite analysis of deep convection and its moist environment over the Indian Ocean during the Winter Monsoon. *J. Geophys. Res.*, **107**, D19, doi:10.1029/2000JD000040.

- Rossow, W. B. and L. C. Garder, 1993: Cloud detection using satellite measurements of infrared and visible radiances for ISCCP. *J. Climate*, **6**, 2341–2369.
- Sherwood, S. C. and R. Wahrlich, 1999: Observed Evolution of Tropical Deep Convective Events and Their Environment. *Mon. Wea. Rev.*, **127**, 1777-1795.
- Slingo, J. M., 1987: The development and verification of a cloud prediction scheme for the ECMWF model. *Quart. J. Roy. Meteor. Soc.*, **113**, 899-927.
- Stowe, L. L., E. P. McClain, R. Carey, P. Pellegrino, and G. G. Gutman, 1991: Global distribution of cloud cover derived from NOAA/AVHRR operational satellite data. *Adv. Space Res.*, **11**, 51–54.
- Sundqvist, H. R., 1988: Parameterization of condensation and associated clouds in models for weather prediction and general circulation simulation. *Physically-Based Modelling and Simulation of Climate and Climatic Change*, M. E. Schlesinger, Ed., Kluwer Academic, 433-461.
- Trenberth, K. E., 1998: Atmospheric Moisture Residence Times and Cycling: Implications for Rainfall Rates and Climate Change. *Climate Change*, **39**, 667-694.
- Wilcox, E. M. and V. Ramanathan, 2001: Scale dependence of the thermodynamic forcing of tropical monsoon clouds: Results from TRMM observations. *J. Climate*, **14**, 1511-1524.
- Williams, M. and R. A. Houze Jr., 1987: Satellite-observed characteristics of Winter Monsoon cloud clusters. *Mon. Wea. Rev.*, **115**, 505-519.
- Zhang, G. J. and N. A. McFarlane, 1995: Sensitivity of climate simulations to the parameterization of cumulus convection in the Canadian Climate Centre General Circulation Model. *Atmos.-Ocean*, **33**, 407-446.

TABLE CAPTIONS

Table 1. METEOSAT-5 pixel classification scheme.

Table 2. Comparison of mean precipitation and cloud properties.

FIGURE CAPTIONS

Figure 1: (a) Sample METEOSAT-5 infrared channel brightness temperature image from 18 Jan 1999 1100 GMT. (b) The same image following the pixel classification stage of the analysis. Red pixels are deep convection/anvil; green pixels are shallow convection/thick cirrus; blue pixels are thin cirrus. (c) The same image following the cloud clustering stage of the analysis.

Figure 2: Scatter plot of cloud area-averaged rain rate (R_c) from TRMM and cloud area fraction colder than 240 K (f_{240}) from METEOSAT-5 for a sample of nearly 350 clouds from January, 1999.

Figure 3: (a) Number distribution of clouds. (b) Cloud area averaged over the lifetime of each cloud. (c) Cumulative contribution to total cloud area. All are shown as a function of cloud lifetime. Solid lines are observed clouds. Dotted lines are simulated clouds. Horizontal dashed line in (b) indicates approximate size of a single model grid cell. Error bars indicate one standard deviation of the mean cloud area in each size bin.

Figure 4: (a) Evolution of cloud area for a single cloud observed over a 7-day period. (b) Evolution of spatial coverage of each cloud type within the cloud. Solid line is deep convection/anvil cloud; dashed line is shallow convective/thick cirrus cloud; dash-dot line is thin cirrus. (c) Evolution of rain rate averaged over the entire area of the cloud. (d) Same as (b) for 24-hour period. Time on axis indicates local time at the geographic center of the cloud.

Figure 5: (a) Number distribution of clouds as a function of cloud area. Solid line is METEOSAT-5 observed clouds and dotted line is simulated clouds. Inset: number distribution of clouds observed by METEOSAT-5 (solid line), TRMM-VIRS (dashed line), TRMM-CERES (dotted line; from Wilcox and Ramanathan 2001). (b) Cumulative contribution to total cloud area as a function of cloud area.

Figure 6: (a) Rain rate averaged over the entire area of cloud. (b) Fraction of clouds in each size bin that contain some precipitation. All are shown as a function of cloud area. Solid lines are observed clouds. Dotted lines are simulated clouds. Error bars indicate one standard deviation of the mean rain rate in each size bin.

Figure 7: (a) Frequency distribution of rain rate. (b) Cumulative contribution to total precipitation. Solid lines are observations from the TRMM Microwave Imager. Dotted lines are simulated rain rates from CCM3. Dashed lines are simulated rain rates from CCM3 with the mesoscale evaporation modification added to the model. All rain rates are averaged over CCM3 grid boxes at T42 resolution.

Table 1. METEOSAT-5 pixel classification scheme

brightness temperature (K)	
deep convection/anvil	$T_{IR} < 240$
Shallow conv./thick cirrus	$240 \leq T_{IR} < 280$
thin cirrus	$T_{IR} \geq 280, T_{WV} < 245$
clear sky or broken cloud*	$T_{IR} \geq 280, T_{WV} > 245$

*not included in the cloud detection or tracking analysis.

Table 2. Comparison of mean precipitation and cloud properties.

	TRMM	METEOSAT-5	CCM3
	observations	observations	simulation
Rain rate (mm day ⁻¹)	3.31	3.25	5.31
Fraction of precipitation from partly cloudy grid cells (%)		32*	19
Cloud cover (%)		45	66
Overcast grid cell cover (%)		27	52
Partially filled grid cell cover (%)		18	14

*from colocated METEOSAT-5 cloud mask and TRMM TMI rain rates.

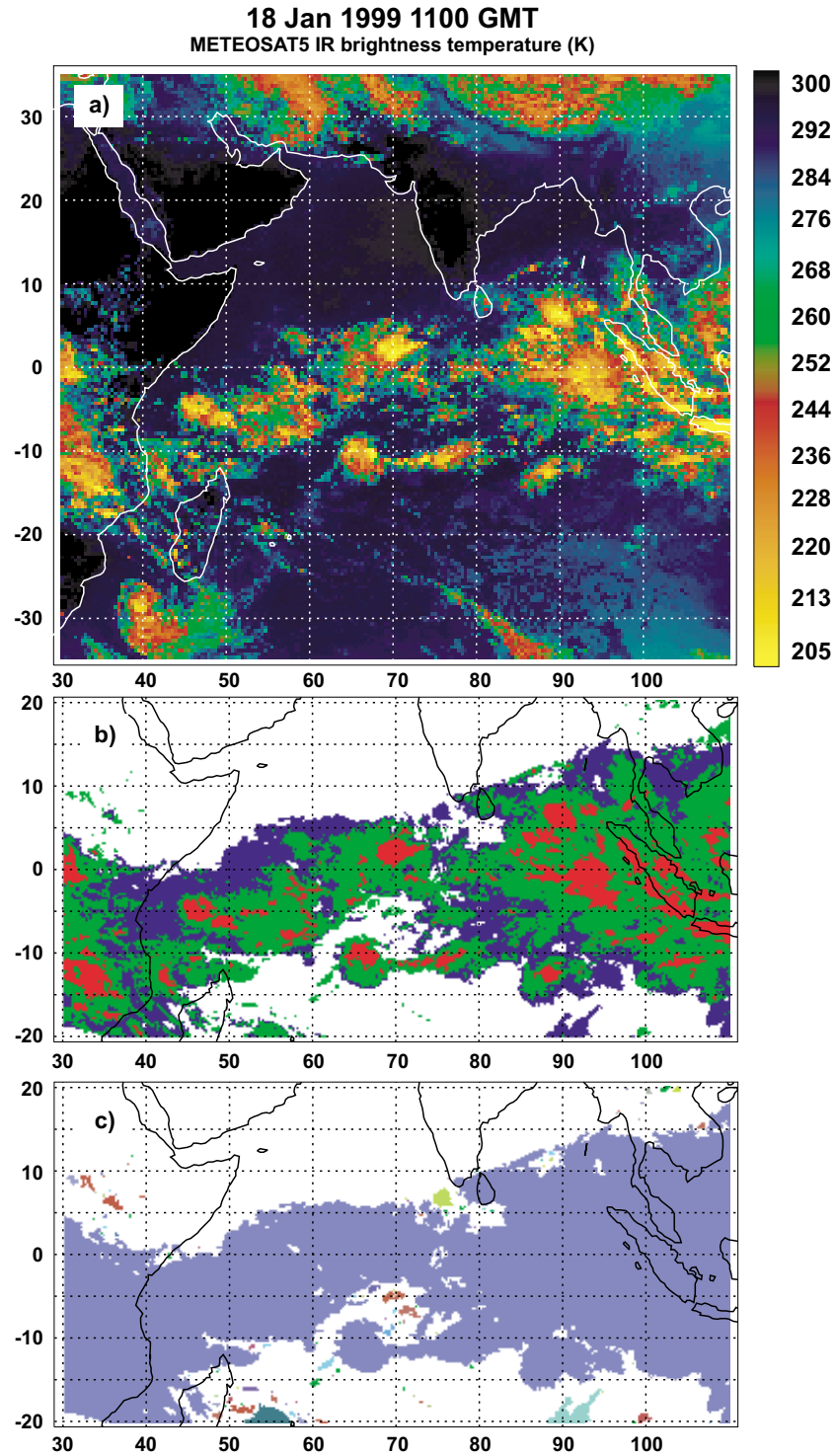


Figure 1: (a) Sample METEOSAT-5 infrared channel brightness temperature image from 18 Jan 1999 1100 GMT. (b) The same image following the pixel classification stage of the analysis. Red pixels are deep convection/anvil; green pixels are shallow convection/thick cirrus; blue pixels are thin cirrus. (c) The same image following the cloud clustering stage of the analysis.

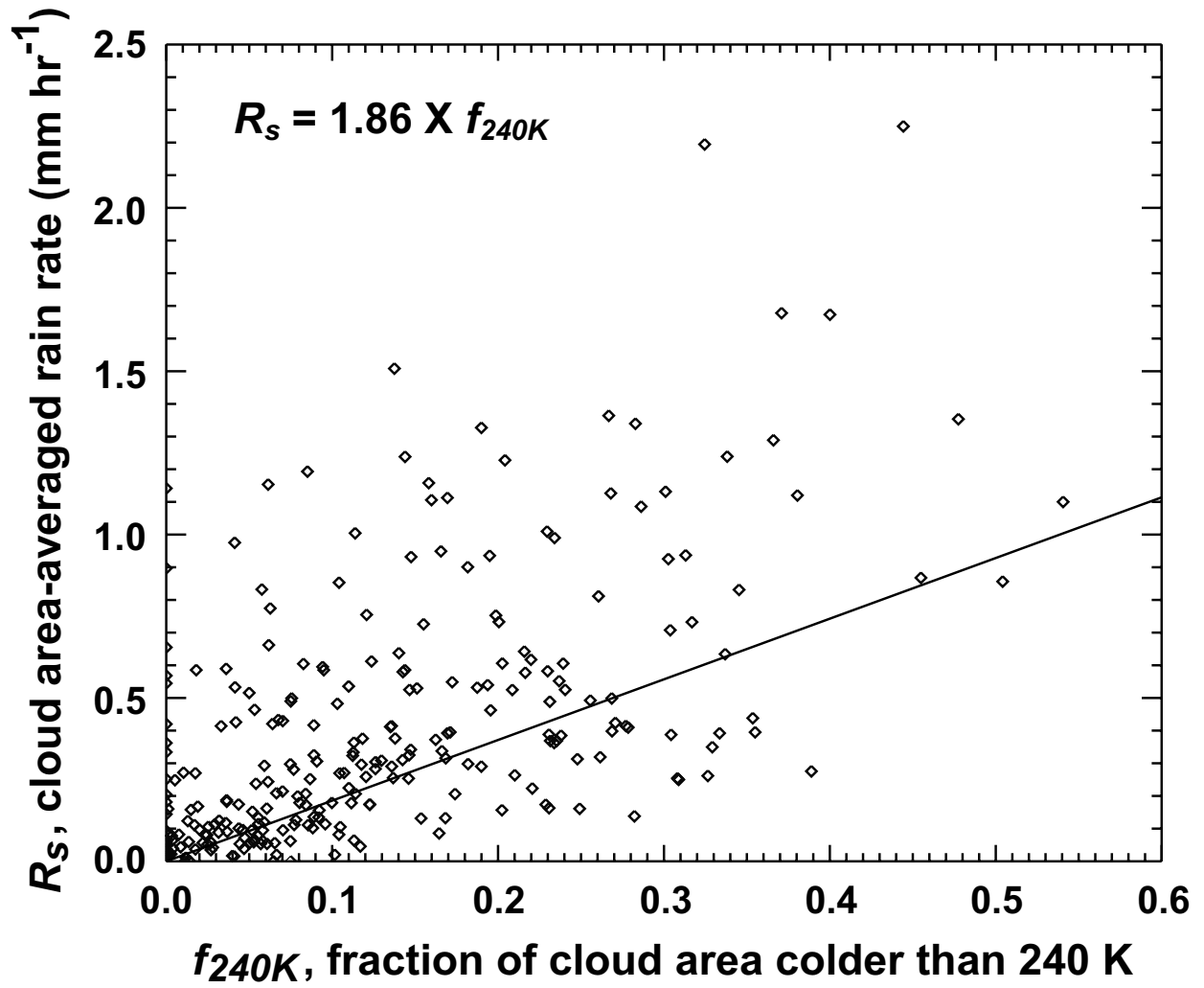


Figure 2: Scatter plot of cloud area-averaged rain rate (R_s) from TRMM and cloud area fraction colder than 240 K (f_{240}) from METEOSAT-5 for a sample of nearly 350 clouds from January, 1999.

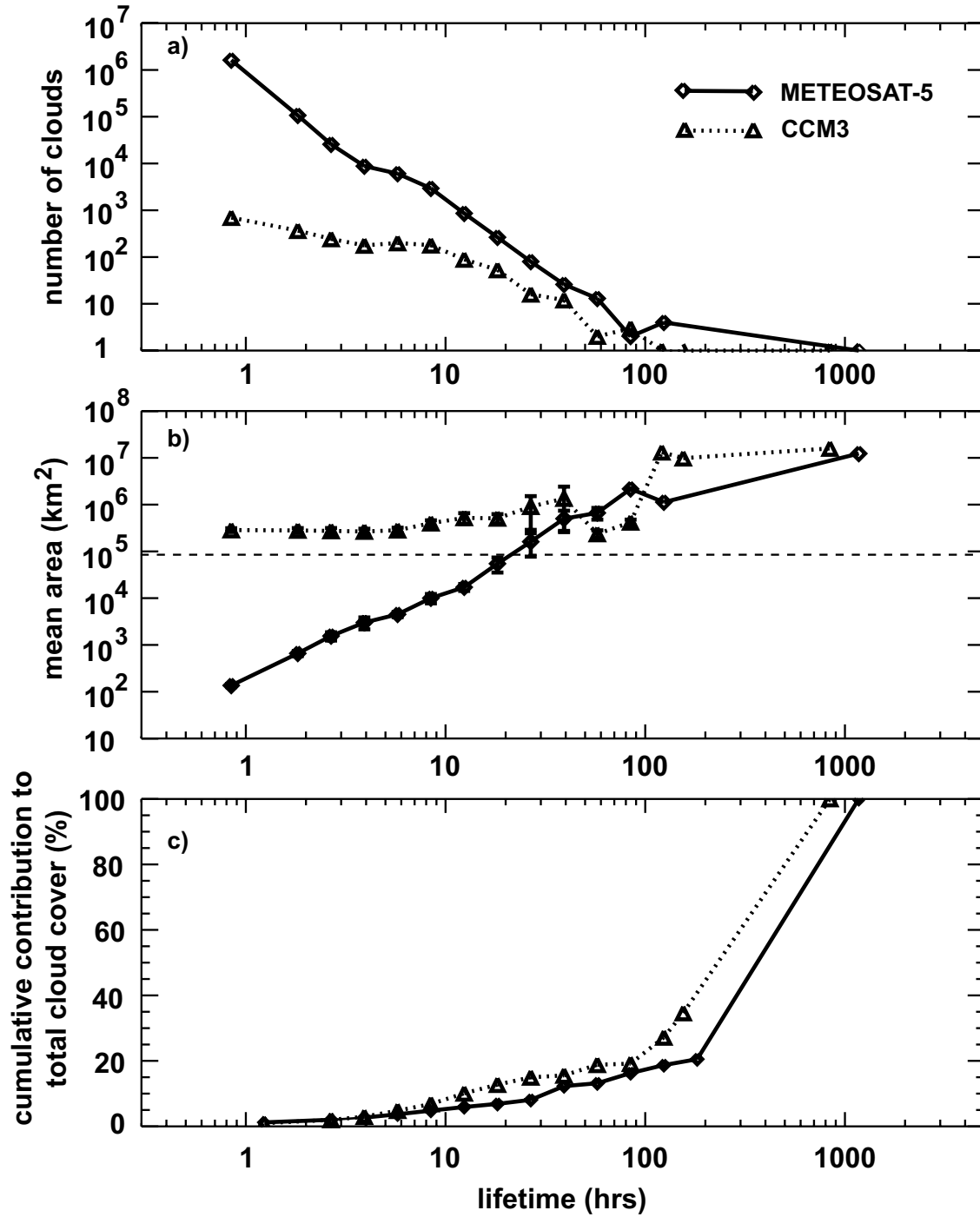


Figure 3: (a) Number distribution of clouds. (b) Cloud area averaged over the lifetime of each cloud. (c) Cumulative contribution to total cloud area. All are shown as a function of cloud lifetime. Solid lines are observed clouds. Dotted lines are simulated clouds. Horizontal dashed line in (b) indicates approximate size of a single model grid cell. Error bars indicate one standard deviation of the mean cloud area in each size bin.

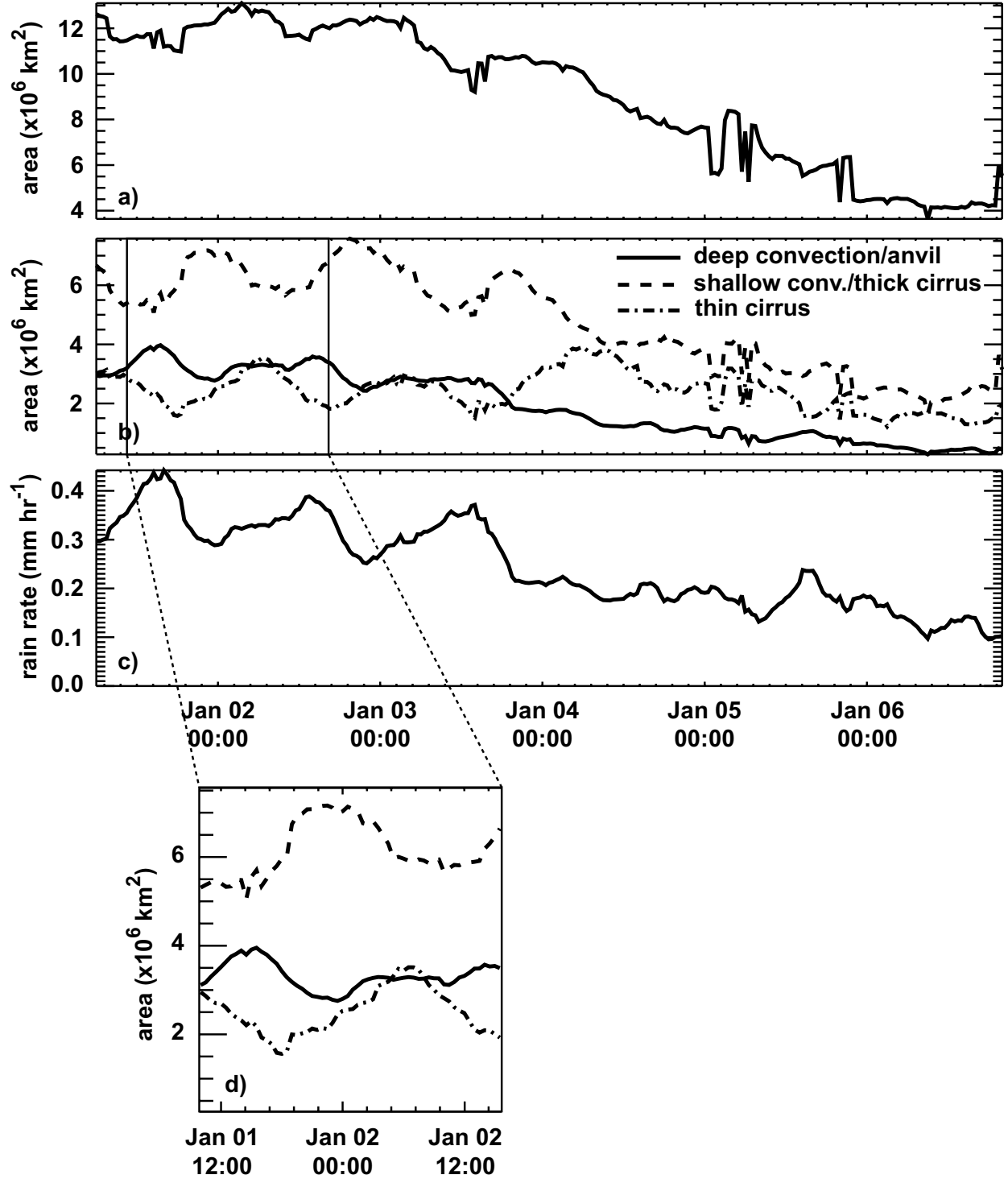


Figure 4: (a) Evolution of cloud area for a single cloud observed over a 7-day period. (b) Evolution of spatial coverage of each cloud type within the cloud. Solid line is deep convection/anvil cloud; dashed line is shallow convective/thick cirrus cloud; dash-dot line is thin cirrus. (c) Evolution of rain rate averaged over the entire area of the cloud. (d) Same as (b) for 24-hour period. Time on axis indicates local time at the geographic center of the cloud.

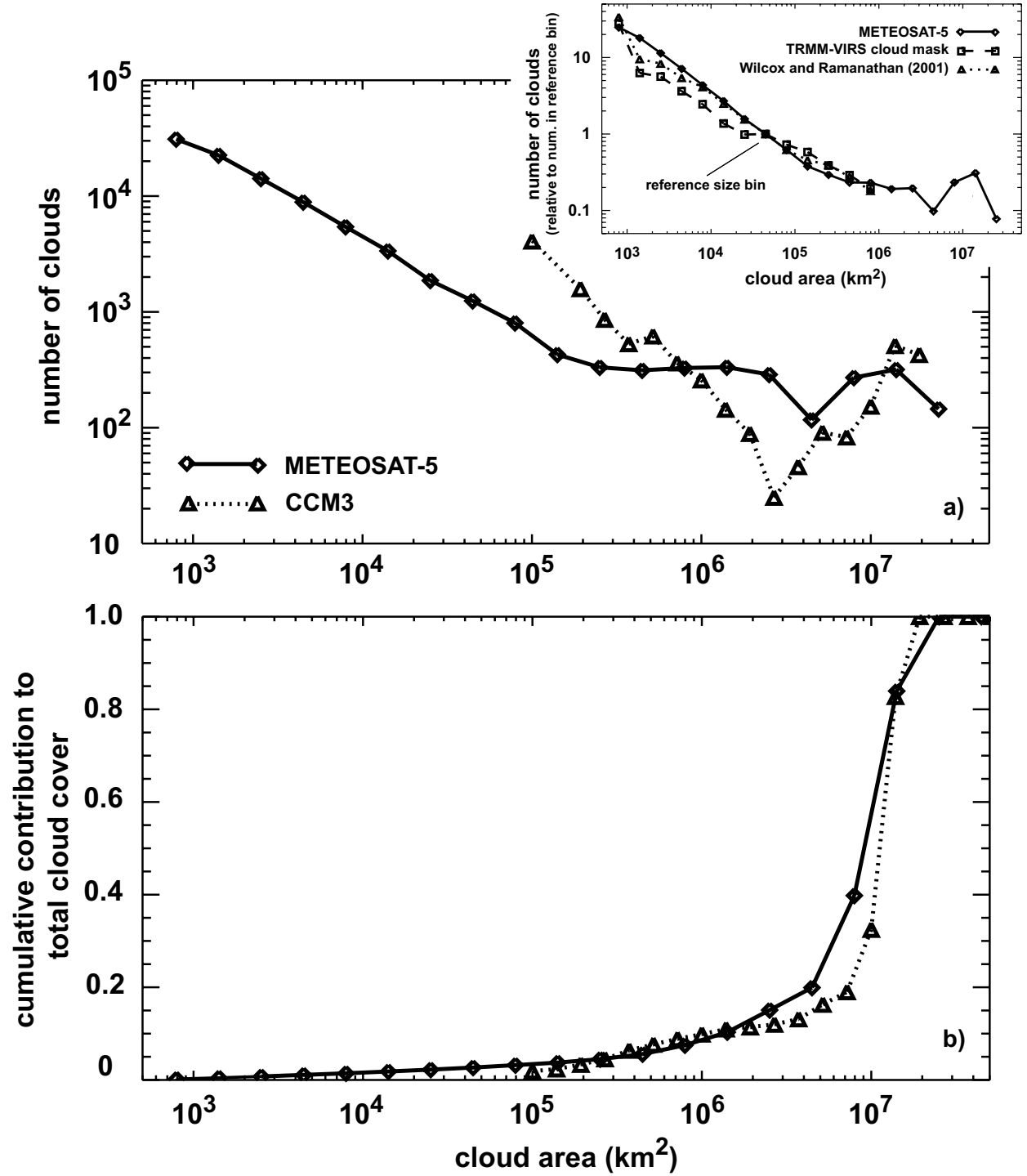


Figure 5: (a) Number distribution of clouds as a function of cloud area. Solid line is METEOSAT-5 observed clouds and dotted line is simulated clouds. Inset: number distribution of clouds observed by METEOSAT-5 (solid line), TRMM-VIRS (dashed line), TRMM-CERES (dotted line; from Wilcox and Ramanathan 2001). (b) Cumulative contribution to total cloud area as a function of cloud area.

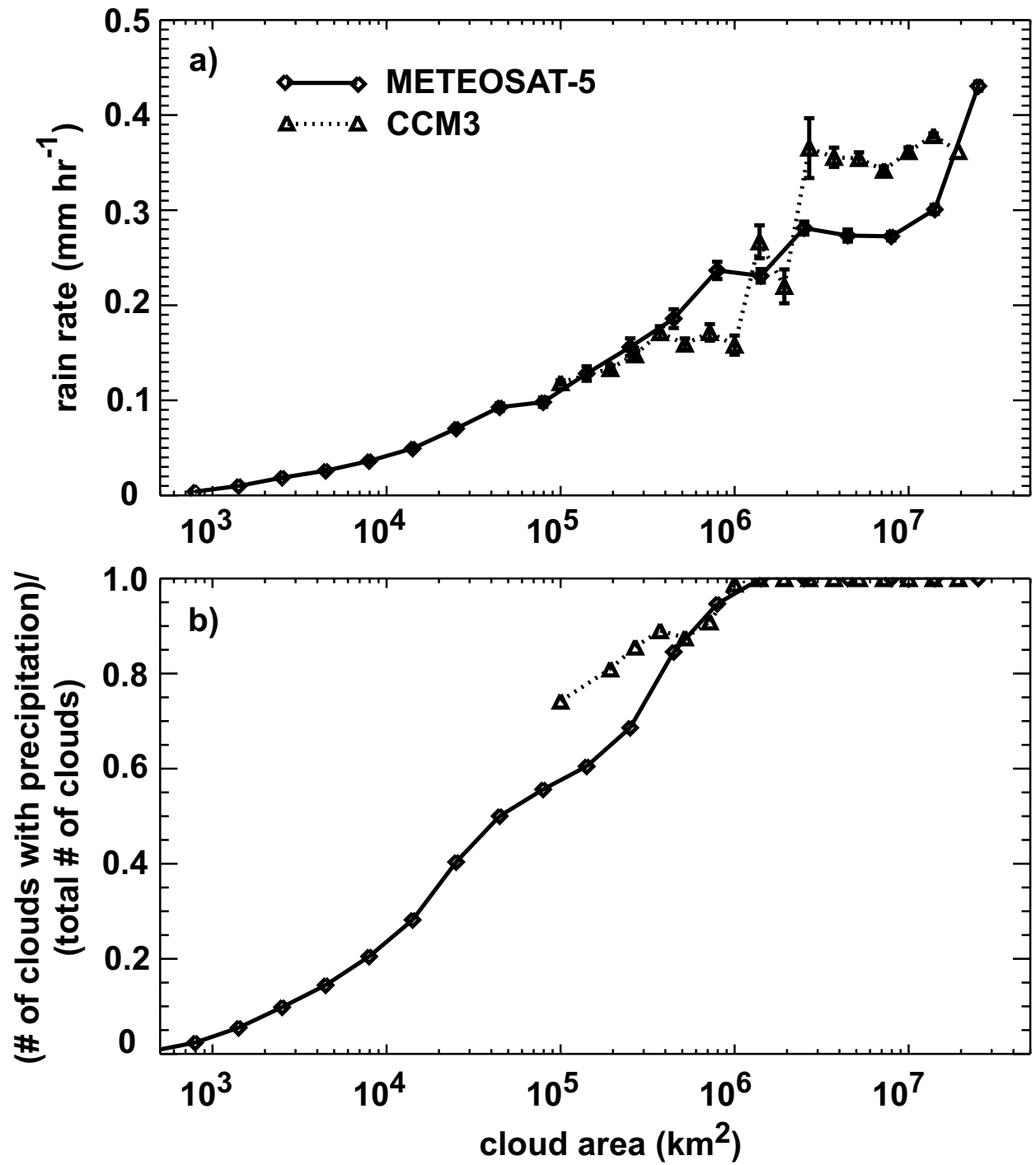


Figure 6: (a) Rain rate averaged over the entire area of cloud. (b) Fraction of clouds in each size bin that contain some precipitation. All are shown as a function of cloud area. Solid lines are observed clouds. Dotted lines are simulated clouds. Error bars indicate one standard deviation of the mean rain rate in each size bin.

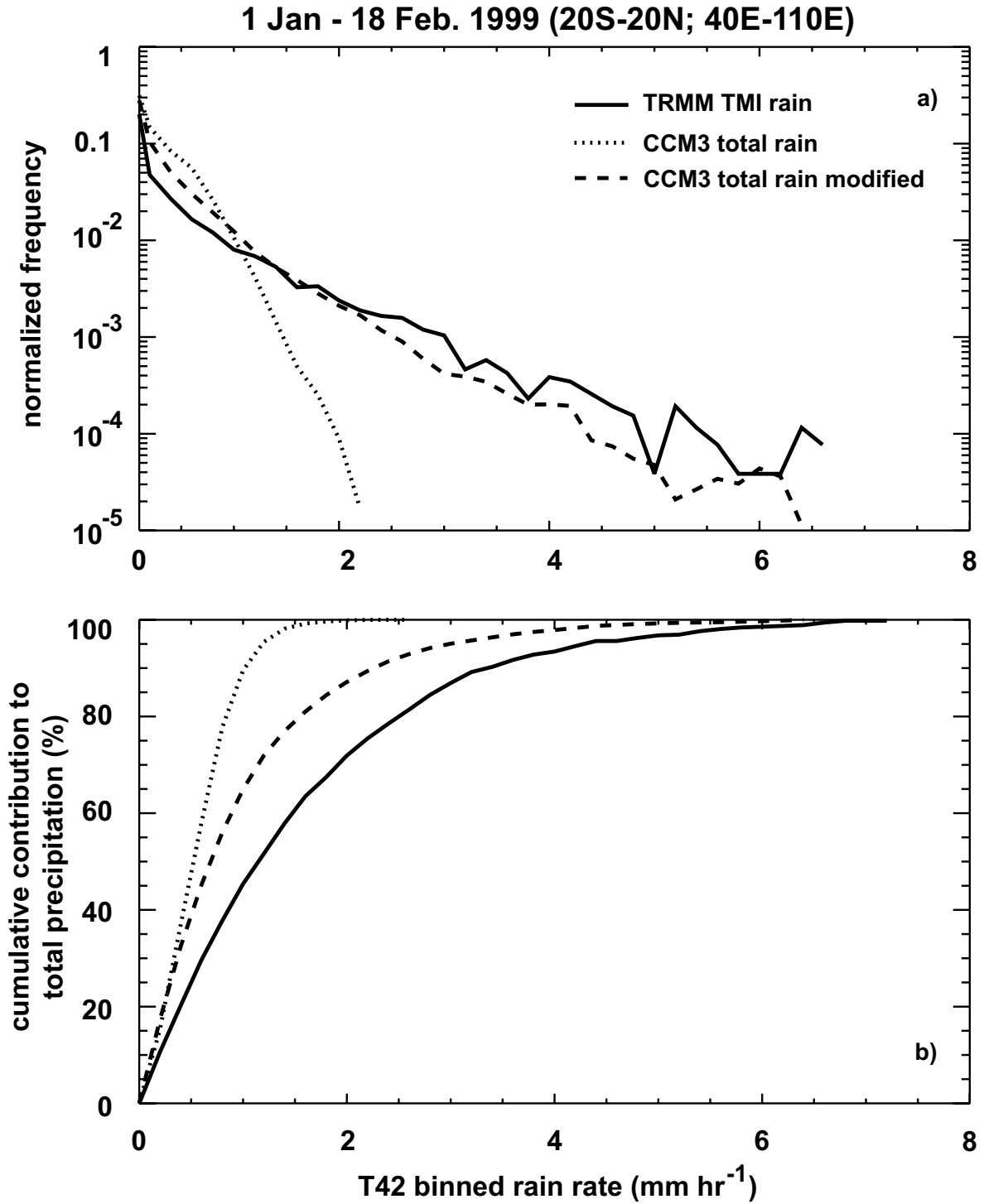


Figure 7: (a) Frequency distribution of rain rate. (b) Cumulative contribution to total precipitation. Solid lines are observations from the TRMM Microwave Imager. Dotted lines are simulated rain rates from CCM3. Dashed lines are simulated rain rates from CCM3 with the mesoscale evaporation modification added to the model. All rain rates are averaged over CCM3 grid boxes at T42 resolution.